Evolution of the Ionizing Background at High Redshifts

Andrew J. Cooke[1], Brian Espey[2] and Bob Carswell[3]

[1] *Institute for Astronomy, Edinburgh, Scotland.*
[2] *The John Hopkins University, Baltimore, USA.*
[3] *Institute of Astronomy, Cambridge, England.*

ABSTRACT

The decrease in number density of Lyman–α clouds near the background quasar is an observational result which is often called the 'proximity' or 'inverse' effect. It is thought that, for nearby clouds, the quasar's flux dominates the background radiation field, increasing the ionization state of the clouds and reducing the (observed) H I column density.

In this paper we analyse a sample of 11 quasars from the literature for which accurate column density estimates of the Lyman–α lines exist. We confirm, to a significance level of more than 3 standard deviations, that the proximity effect exists. If it is related to the background flux then the intensity and evolution of the background have been constrained.

Using a maximum likelihood method, we determine the strength of the extragalactic ionizing background for $2.0 < z < 4.5$, taking account of possible systematic errors in our determination and estimating the effect of biases inherent in the data. If the background is constant we find that it has an intensity of 100^{+50}_{-30} J_{23}, where J_{23} is defined as 10^{-23} ergs cm^{-2} Hz^{-1} sr^{-1}. There is no significant evidence for a change in this value with redshift.

Key words: cosmology: diffuse radiation – quasars: absorption lines – galaxies: evolution

1   INTRODUCTION

1.1   The Lyman–alpha forest

Spectroscopic observations towards quasars show a large number of intervening absorption systems. This 'forest' of lines is numerically dominated by systems showing only the Lyman–alpha transition — these absorbers are called Lyman alpha clouds.

Earlier work suggests that the clouds are large, highly ionized structures, either pressure confined (eg. Ostriker & Ikeuchi 1983) or within cold dark matter structures (eg. Miralda–Escudé & Rees 1993; Cen, Miralda–Escudé & Ostriker 1994; Petitjean & Mücket 1995; Zhang, Anninos & Norman 1995). However, alternative models do exist: cold, pressure confined clouds (eg. Barcons & Fabian 1987, but see Rauch et al. 1993); various shock mechanisms (Vishniac & Bust 1987, Hogan 1987).

Low and medium resolution spectroscopic studies of the forest generally measure the redshift and equivalent width of each cloud. At higher resolutions it is possible to measure the redshift (z), H I column density (N, atoms per cm^2) and Doppler parameter (b, km s^{-1}). These are obtained by fitting a Voigt profile to the data (Rybicki & Lightman 1979).

Using a list of N, z and b measurements, and their associated error estimates, the number density of the population can be studied. Most work has assumed that the density is a separable function of z, N and b (Rauch et al. 1993).

There is a local decrease in cloud numbers near the background quasar which is normally attributed to the additional ionizing flux in that region. While this may not be the only reason for the depletion (the environment near quasars may be different in other respects; the cloud redshifts may reflect systematic motions) it is expected for the standard physical models wherever the ionising flux from the quasar exceeds, or is comparable to, the background.

Since the generally accepted cloud models are both optically thin to ionizing radiation and highly ionized, it is possible to correct column densities from the observed values to those that would be seen if the quasar were more remote. The simplest correction assumes that the shape of the two incident spectra — quasar and background — are similar. In this case the column density of the neutral fraction is inversely proportional to the incident ionizing flux.

If the flux from the quasar is known, and the depletion of clouds is measured from observations, the background flux can be determined. By observing absorption towards quasars

at different redshifts the evolution of the flux can be measured. Bechtold (1993) summarises earlier measurements of the ionising flux, both locally and at higher redshifts.

Recently Loeb & Eisenstein (1995) have suggested that enhanced clustering near quasars causes this approach to overestimate the background flux. If this is the case then an analysis which can also study the evolution of the effect gives important information. In particular, a decrease in the inferred flux might be expected after the redshift where the quasar population appears to decrease. However, if the postulated clustering enhancement is related to the turn–on of quasars at high redshift, it may conspire to mask any change in the ionizing background.

Section 2 describes the model of the population density in more detail, including the corrections to flux and redshift that are necessary for a reliable result. The data used are described in section 3. In section 4 the quality of the fit is assessed and the procedure used to calculate errors in the derived parameters is explained. Results are given in section 5 and their implications discussed in section 6. Section 7 concludes the paper.

2   THE MODEL

2.1   Population Density

The Doppler parameter distribution is not included in the model since it is not needed to determine the ionizing background from the proximity effect. The model here assumes that N and z are uncorrelated. While this is unlikely (Carswell 1995), it should be a good approximation over the restricted range of column densities considered here.

The model of the population without Doppler parameters or the correction for the proximity effect is

$$dn(N', z) = A'(1+z)^{\gamma'} (N')^{-\beta} \frac{c(1+z)}{H_0(1+2q_0 z)^{\frac{1}{2}}} \, dN' \, dz \quad (1)$$

where H_0 is the Hubble parameter, q_0 is the cosmological deceleration parameter and c is the speed of light. Correcting for the ionizing flux and changing from 'original' (N') to 'observed' (N) column densities, gives

$$dn(N, z) = A(1+z)^{\gamma'} \left(\frac{N}{\Delta_F}\right)^{-\beta} \frac{c(1+z)}{H_0(1+2q_0 z)^{\frac{1}{2}}} \frac{dN}{\Delta_F} \, dz \quad (2)$$

where

$$N = N'\Delta_F \,, \tag{3}$$

$$\Delta_F = \frac{f_\nu^B}{f_\nu^B + f_\nu^Q} \,, \tag{4}$$

and f_ν^B is the background flux, f_ν^Q is the flux from the quasar ($4\pi J_\nu(z)$).

The background flux J_ν^B may vary with redshift. Here it is parameterised as a constant, a power law, or two power laws with a break which is fixed at $z_B = 3.25$ (the mid–point of the available data range). An attempt was made to fit models with z_B as a free parameter, but the models were too poorly constrained by the data to be useful.

$$J_\nu(z) = 10^{J_{3.25}} \quad \text{model } \mathbf{B} \qquad (5)$$

$$J_\nu(z) = 10^{J_{3.25}} \left(\frac{1+z}{1+3.25}\right)^{\alpha_1} \qquad \mathbf{C} \qquad (6)$$

$$J_\nu(z) = 10^{J_{z_B}} \times \left\{ \begin{array}{ll} \left(\frac{1+z}{1+z_B}\right)^{\alpha_1} & z < z_B \\ \left(\frac{1+z}{1+z_B}\right)^{\alpha_2} & z > z_B \end{array} \right. \qquad \mathbf{D \ \& \ E} \qquad (7)$$

A large amount of information (figure 3) is used to constrain the model parameters. The high–resolution line lists give the column density and redshift, with associated errors, for each line. To calculate the background ionising flux the quasar luminosity and redshift must be known (table 2). Finally, each set of lines must have observational completeness limits (table 3).

2.2   Malmquist Bias and Line Blending

Malmquist bias is a common problem when fitting models to a population which increases rapidly at some point (often near an observational limit). Errors during the observations scatter lines away from the more populated regions of parameter space and into less populated areas. Line blending occurs when, especially at high redshifts, nearby, overlapping lines cannot be individually resolved. This is a consequence of the natural line width of the clouds and cannot be corrected with improved spectrographic resolution. The end result is that weaker lines are not detected in the resultant 'blend'. Both these effects mean that the observed population is not identical to the 'underlying' or 'real' distribution.

2.2.1   The Idea of Data Quality

To calculate a correction for Malmquist bias we need to understand the significance of the error estimate since any correction involves understanding what would happen if the 'same' error occurs for different column density clouds. The same physical cloud cannot be observed with completely different parameters, but the same combination of all the complex factors which influence the errors might affect a line with different parameters in a predictable way. If this idea of the 'quality' of an observation could be quantified it would be possible to correct for Malmquist bias: rather than the 'underlying' population, one reflecting the quality of the observation (ie. including the bias due to observational errors) could be fitted to the data.

For example, if the 'quality' of an observation was such that, whatever the actual column density measured, the error in column density was the same, then it would be trivial to convolve the 'underlying' model with a Gaussian of the correct width to arrive at an 'observed' model. Fitting the latter to the data would give parameters unaffected by Malmquist bias. Another example is the case of galaxy magnitudes. The error in a measured magnitude is a fairly simple function of source brightness, exposure time, etc., and so it is possible to correct a flux–limited galaxy survey for Malmquist bias.

2.2.2   Using Errors as a Measure of Quality

It may be possible to describe the quality of a spectrum by the signal to noise level in each bin. From this one could, for a given line, calculate the expected error in the equivalent width. The error in the equivalent width might translate,
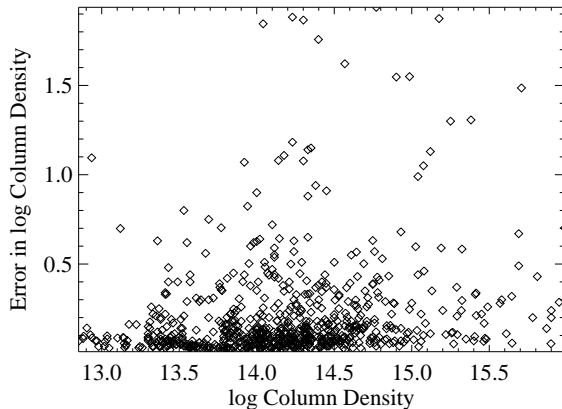
Figure 1. The distribution of errors in column density.

Figure 2. A model including Malmquist bias. The bold, solid line is the original sample, the bold, dashed line is the distribution after processing as described in the text. Each curve is shown twice, but the upper right plot has both axes scaled by a factor of 3 and only shows data for $12.5 < \log(N) < 16$. Reference lines showing the evolution expected for $\beta = 1.5$ and 1.45 (dashed) are also shown (centre).

depending on whether the absorption line was in the linear or logarithmic portion of the 'curve of growth', to a normal error in either N or $\log(N)$. But in this idealised case it has been assumed that the spectrum has not been re–binned, leaving the errors uncorrelated; that the effect of overlapping, blended lines is unimportant; that there is a sudden transition from a linear to logarithmic curve of growth; that the resulting error is well described by a normal distribution. None of this is likely to be correct and, in any case, the resulting analysis, with different 'observed' populations for every line, would be too unwieldy to implement, given current computing facilities.

A more pragmatic approach might be possible. A plot of the distribution of errors with column density (figure 1) suggests that the errors in $\log(N)$ are of a similar magnitude for a wide range of lines (although there is a significant correlation between the two parameters). Could the error in $\log(N)$ be a sufficiently good indicator of the 'quality' of an observation?

If the number density of the underlying population is $n'(N) \, \mathrm{d}\log(N)$ then the observed population density for a line with error in $\log(N)$ of σ_N is:

$$n(N) \, \mathrm{d}\log(N) \propto \int_{-\infty}^{\infty} n' \left(N 10^x \right) \exp\left(\frac{-x^2}{2\sigma_N^2} \right) \, \mathrm{d}x \; . \qquad (8)$$

For a power law distribution this can be calculated analytically and gives an increased probability of seeing lines with larger errors, as expected. For an underlying population density $N^{-\beta} \, \mathrm{d}N$ the increase is $\exp\left((1-\beta)^2 (\sigma_N \log 10)^2 / 2 \right)$.

This gives a lower statistical weight to lines with larger errors when fitting. For this case — a power law and log–normal errors — the weighting is not a function of N directly, which might imply that any correction would be uniform, with little bias expected for estimated parameters.

In practice this correction does not work. This is probably because the exponential dependence of the correction on σ_N makes it extremely sensitive to the assumptions made in the derivation above. These assumptions are not correct. For example, it seems that the correlation between $\log(N)$ and the associated error is important.
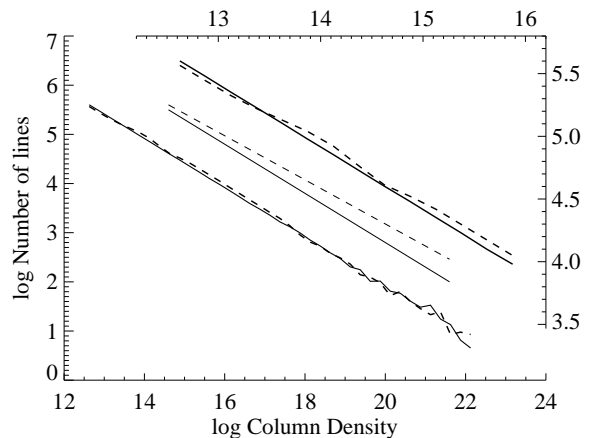
2.2.3   An Estimation of the Malmquist Bias

It is possible to do a simple numerical simulation to gauge the magnitude of the effect of Malmquist bias. A population of ten million column densities were selected at random from a power law distribution ($\beta = 1.5, \log(N_{\min}) = 10.9, \log(N_{\max}) = 22.5$) as an 'unbiased' sample. Each line was given an 'observed' column density by adding a random error distributed with a normal or log–normal (for lines where $13.8 < \log(N) < 17.8$) distribution, with a mean of zero and a standard deviation in $\log(N)$ of 0.5. This procedure is a simple approximation to the type of errors coming from the curve of growth analysis discussed above, assuming that errors are approximately constant in $\log(N)$ (figure 1). The size of the error is larger than typical, so any inferred change in β should be an upper limit.

Since a power–law distribution diverges as $N \to 0$ a normal distribution of errors in N would give an infinite number of observed lines at every column density. This is clearly unphysical (presumably the errors are not as extended as in a normal distribution and the population has some low column density limit). Because of this the 'normal' errors above were actually constrained to lie within 3 standard deviations of zero.

The results (figure 2) show that Malmquist bias has only a small effect, at least for the model used here. The main solid line is the original sample, the dashed line is the observed population. Note that the results in this paper come from fitting to a sample of lines with $12.5 < \log(N) < 16$ (section 3) — corresponding to the data shown expanded to the upper right of the figure. Lines with smaller column densities are not shown since that fraction of the population is affected by the lower density cut–off in the synthetic data.

A comparison with the two reference lines, showing the slopes for a population with $\beta = 1.5$ or 1.45 (dashed), indicates that the expected change in β is ~ 0.05. The population of lines within the logarithmic region of the curve of growth appears to be slightly enhanced, but otherwise the

two curves are remarkably similar. The variations at large column densities are due to the small number of strong lines in the sample.

2.2.4   Other Approaches

What other approaches can be used to measure or correct the effects of Malmquist bias and line blending? Press & Rybicki (1993) used a completely different analysis of the Lyman–α forest. Generating and reducing synthetic data, with a known background and cloud population, would allow us to assess the effect of blending. Changing (sub–setting) the sample of lines that is analysed will alter the relative (and, possibly, absolute) importance of the two effects.

The procedure used by Press & Rybicki (1993) is not affected by Malmquist bias or line blending, but it is difficult to adapt to measure the ionizing background.

Profile fitting to high–resolution data is a slow process, involving significant manual intervention (we have tried to automate profile–fitting with little success). An accurate measurement of the systematic error in the ionizing background would need an order of magnitude more data than is used here to get sufficiently low error limits. Even if this is possible — the analysis would need a prohibitive amount of CPU time — it would be sufficient work for a separate, major paper (we would be glad to supply our software to anyone willing to try this).

Taking a sub–set of the data is not helpful unless it is less likely to be affected by the biases described above. One approach might be to reject points with large errors, or large relative errors, in column density since these are more affected by Malmquist bias. However, this would make the observations incomplete in a very poorly understood way. For example, relative errors are correlated with column density (as noted above) and so rejecting lines with larger relative errors would preferentially reject higher column density lines. There is no sense in trying to measure one bias if doing so introduces others.

Unlike rejecting lines throughout the sample, changing the completeness limit does not alter the coverage of the observations (or rather, it does so in a way that is understood and corrected for within the analysis). Raising the completeness limits should make line blending less important since weaker lines, which are most likely to be blended, are excluded from the fit. Whether it affects the Malmquist bias depends on the distribution of errors.

For blended lines, which tend to be weak, raising the completeness limit should increase the absolute value of β since the more populous region of the (hypothetical) power–law population of column densities will no longer be artificially depleted. The effect on γ is more difficult to assess since it is uncertain whether the completeness limits are correct at each redshift. If the limits increase too rapidly with redshift, for example, then raising them further will reduce blending most at lower redshifts, lowering γ. But if they are increasing too slowly then the converse will be true.

2.2.5   Conclusions

Until either profile–fitting is automated, or the method of Press & Rybicki (1993) can be modified to include the proximity effect, these two sources of uncertainty — Malmquist bias and line blending — will continue be a problem for any analysis of the Lyman–α forest. However, from the arguments above, it is likely that the effect of Malmquist bias is small and that, by increasing the completeness limit, we can assess the magnitude of the effect of line blending.

2.3   Flux Calculations

2.3.1   Galactic Extinction

Extinction within our Galaxy reduces the apparent luminosity of the quasars and so lowers the estimate of the background. Since the absorption varies with frequency this also alters the observed spectral slope.

Observed fluxes were corrected using extinction estimates derived from the H I measurements of Heiles & Cleary (1979) for Q2204–573 and Stark et al. (1992) for all the other objects. H I column densities were converted to $E(B-V)$ using the relationships:

$$E(B-V) \quad = \quad \frac{N_{\text{H I}}}{5.27\,10^{21}} \quad \text{if } \frac{N_{\text{H I}}}{5.27\,10^{21}} < 0.1 \qquad (9)$$

$$E(B-V) \quad = \quad \frac{N_{\text{H I}}}{4.37\,10^{21}} \quad \text{otherwise} \qquad (10)$$

where the first value comes from Diplas & Savage (1994) and the second value, which compensates for the presence of H_2, is the first scaled by the ratio of the conversions given in Bohlin, Savage & Drake (1978). A ratio $R = A(V)/E(B-V)$ of 3.0 (Lockman & Savage 1995) was used and variations of extinction with frequency, $A(\lambda)/A(V)$ were taken from Cardelli, Clayton & Mathis (1989).

The correction to the observed index, α_o, of the power–law continuum,

$$f_\nu \propto \nu^{-\alpha} \, , \qquad (11)$$

was calculated using

$$\alpha_o = \alpha + \frac{A(V)}{2.5} \frac{\partial}{\partial \ln \nu} \frac{A(\nu)}{A(V)} \qquad (12)$$

which, using the notation of Cardelli, Clayton & Mathis (1989), becomes

$$\alpha_o = \alpha + \frac{A(V)}{2.5\,10^6 c} \nu \ln(10) \frac{\partial}{\partial y} \left(a(x) + \frac{b(x)}{R} \right) \, . \qquad (13)$$

2.3.2   Extinction in Damped Systems

Two quasars are known to have damped absorption systems along the line of sight (Wolfe et al. 1995). The extinction due to these systems is not certain, but model **E** includes the corrections listed in table 1. These have been calculated using the SMC extinction curve in Pei (1992), with a correction for the evolution of heavy element abundances taken from Pei & Fall (1995). The SMC extinction curve is most suitable for these systems since they do not appear to have structure at 2220 Å (Boissé & Bergeron 1988), unlike LMC and Galactic curves.

2.3.3   Absorption by Clouds near the Quasar

The amount of ionizing flux from the background quasar incident on a cloud is attenuated by all the other clouds

Object	$\log(N_{\text{H I}})$	z_{abs}	$A(V)$	Δ_α
Q0000–263	21.3	3.39	0.10	0.078
Q2206–199	20.7	1.92	0.14	0.10
	20.4	2.08	0.019	0.049

Table 1. The damped absorption systems and associated corrections (at 1450 Å in the quasar's rest–frame) for model **E**.

towards the source. If one of the intervening clouds has a large column density this can significantly reduce the extent of the effect of the quasar.

To correct for this the fraction of ionizing photons from the quasar not attenuated by the intervening H I and He II absorption is estimated before fitting the model. A power–law spectrum is assumed and the attenuation is calculated for each cloud using the cross–sections given in Osterbrock (1989). The ratio $n(\text{He II})/n(\text{H I})$ within the clouds will depend on several unknown factors (the true energy distribution of the ionizing flux, cloud density, etc.), but was assumed to be 10 (Sargent et al. 1980, Miralda–Escudé 1993).

The attenuation is calculated using all the observed intervening clouds. This includes clouds which are not included in the main fit because they lie outside the column density limits, or are too close to the quasar ($\Delta z \leq 0.003$).

For most clouds ($\log(N) \sim 13.5$) near enough to the quasar to influence the calculation of the background this correction is unimportant (less than 1%). However, large ($\log(N) \sim 18$ or larger) clouds attenuate the flux to near zero. This explains why clouds with $\Delta_f \sim 1$ are apparent close to the QSO in figure 11.

This relatively sudden change in optical depth at $\log(N) \sim 18$ is convenient since it makes the correction insensitive to any uncertainties in the calculation (eg. $n(\text{He II})/n(\text{H I})$, the shape of the incident spectrum, absorption by heavier elements) — for most column densities any reasonable model is either insignificant ($\log(N) < 17$) or blocks practically all ionizing radiation ($\log(N) > 19$).

In fact, the simple correction described above is in reasonable agreement with CLOUDY models, for even the most critical column densities. A model cloud with a column density of $\log(N) = 13.5$ and constant density was irradiated by an ionizing spectrum based on that of Haardt & Madau (1996). Between the cloud and quasar the model included an additional absorber (constant density, $\log(N) = 18$) which modified the quasar's spectrum. The effect of the absorber (for a range of heavy element abundances from pure H to primordial to 0.1 solar) on the ionized fraction of H I was consistent with an inferred decrease in the quasar flux of about 80%. In comparison, the correction above, using a power–law spectrum with $\alpha = 1$, gave a reduction of 60% in the quasar flux. These two values are in good agreement, considering the exponential dependence on column densities and the uncertainty in spectral shape. At higher and lower absorber column densities the agreement was even better, as expected.

2.4 Redshift Corrections

Gaskell (1982) first pointed out a discrepancy between the redshifts measured from Lyman α and C IV emission, and those from lower ionization lines (eg. Mg II, the Balmer series). Lower ionization lines have a larger redshift. If the

systemic redshift of the quasar is assumed to be that of the extended emission (Heckman et al. 1991), molecular emission (Barvainis et al. 1994), or forbidden line emission (Carswell et al. 1991), then the low ionization lines give a better measure of the rest–frame redshift.

Using high ionization lines gives a reduced redshift for the quasar, implies a higher incident flux on the clouds from the quasar, and, for the same local depletion of lines, a higher estimate of the background.

Espey (1993) re–analysed the data in Lu, Wolfe & Turnshek (1991), correcting systematic errors in the quasar redshifts. The analysis also considered corrections for optically thick and thin universes and the differences between the background and quasar spectra, but the dominant effect in reducing the estimate from 174 to 50 J_{23} was the change in the quasar redshifts.

To derive a more accurate estimate of the systemic velocity of the quasars in our sample we made use of published redshift measurements of low ionization lines, or measured these where spectra were available to us. The lines used depended on the redshift and line strengths in the data, but typically were one or more of Mg II 2798 Å, O I 1304 Å, and C II 1335 Å.

When no low ionization line observations were available (Q0420–388, Q1158–187, Q2204–573) we applied a mean correction to the high ionization line redshifts. These corrections are based on measurements of the relative velocity shifts between high and low ionization lines in a large sample of quasars (Espey & Junkkarinen 1996). They find a correlation between quasar luminosity and mean velocity difference (Δ_v) with an empirical relationship given by:

$$\Delta_v = \exp(0.66 \log L_{1450} - 13.72) \text{ km s}^{-1} \qquad (14)$$

where L_{1450} is the rest–frame luminosity (ergs Hz^{-1} s^{-1}) of the quasar at 1450 Å for $q_0 = 0.5$ and $H_0 = 100$ km s^{-1}/Mpc.

3 THE DATA

Objects, redshifts and fluxes are listed in table 2. A total of 1675 lines from 11 quasar spectra were taken from the literature. Of these, 844 lie within the range of redshifts and column densities listed in table 3, although the full sample is used to correct for absorption between the quasar and individual clouds (section 2.3.3). The lower column density limits are taken from the references; upper column densities are fixed at $\log(N) = 16$ to avoid the double power law distribution discussed by Petitjean et al. (1993). Fluxes are calculated using standard formulae, assuming a power law spectrum ($f_\nu \propto \nu^{-\alpha}$), with corrections for reddening. Low ionization line redshifts were used where possible, otherwise high ionization lines were corrected using the relation given in section 2.4. Values of α uncorrected for absorption are used where possible, corrected using the relation above. If no α was available, a value of 0.5 was assumed (Francis 1993).

References and notes on the calculations for each object follow:

  Q0000–263 Line list from Cooke (1994). There is some uncertainty in the wavelength calibration for these data, but the error (~ 30km s^{-1}) is much less than the uncertainty

| | | | $L_\nu(1450)$ | | Typical change in $\log(J_{23})$ | | | |
Object	z	α	$q_0 = 0$	$q_0 = 0.5$	z	f_ν	α	Total
Q0000–263	4.124	1.02	13.5×10^{31}	2.8×10^{31}	−0.09	+0.02	+0.01	−0.05
Q0014+813	3.398	0.55	34.0×10^{31}	8.6×10^{31}	−0.19	+0.33	+0.21	+0.36
Q0207–398	2.821	0.41	5.6×10^{31}	1.7×10^{31}	−0.16	+0.03	+0.02	−0.11
Q0420–388	3.124	0.38	10.9×10^{31}	3.0×10^{31}	−0.16	+0.04	+0.02	−0.10
Q1033–033	4.509	0.46	5.5×10^{31}	1.0×10^{31}	−0.05	+0.12	+0.00	+0.06
Q1100–264	2.152	0.34	13.8×10^{31}	5.3×10^{31}	−0.42	+0.19	+0.11	−0.13
Q1158–187	2.454	0.50	42.2×10^{31}	14.4×10^{31}	−0.46	+0.09	+0.06	−0.31
Q1448–232	2.223	0.61	9.6×10^{31}	3.5×10^{31}	−0.34	+0.28	+0.17	+0.11
Q2000–330	3.783	0.85	12.7×10^{31}	2.9×10^{31}	−0.10	+0.16	+0.10	+0.15
Q2204–573	2.731	0.50	42.8×10^{31}	13.3×10^{31}	−0.35	+0.06	+0.03	−0.25
Q2206–199	2.574	0.50	19.4×10^{31}	6.3×10^{31}	−0.31	+0.05	+0.03	−0.22
Mean	3.081	0.56	19.1×10^{31}	5.7×10^{31}	−0.24	+0.12	+0.07	−0.04

Table 2. The systemic redshifts, power law continuum exponents. and rest frame luminosities (ergs $\mathrm{Hz}^{-1}\,\mathrm{s}^{-1}$ at 1450 Å) for the quasars used. $H_0 = 100$ km s^{-1}/Mpc and luminosity scales as H_0^{-2}. The final four columns are an estimate of the relative effect of the various corrections in the paper (systemic redshift, correction for reddening to flux and spectral slope).

in the quasar redshift ($\sim 900 \mathrm{km\,s}^{-1}$) which is taken into account in the error estimate (section 4.2). Redshift this paper (section 2.4). Flux and α measurements from Sargent, Steidel & Boksenberg (1989).

Q0014+813 Line list from Rauch et al. (1993). Redshift this paper (section 2.4). Flux and α measurements from Sargent, Steidel & Boksenberg (1989).

Q0207–398 Line list from Webb (1987). Redshift (O I line) from Wilkes (1984). Flux and α measurements from Baldwin et al. (1995).

Q0420–388 Line list from Atwood, Baldwin & Carswell (1985). Redshift, flux and α from Osmer (1979) (flux measured from plot). The redshifts quoted in the literature vary significantly, so a larger error (0.01) was used in section 4.2.

Q1033–033 Line list and flux from Williger et al. (1994). From their data, $\alpha = 0.78$, without a reddening correction. Redshift this paper (section 2.4).

Q1100–264 Line list from Cooke (1994). Redshift from Espey et al. (1989) and α from Tytler & Fan (1992). Flux measured from Osmer & Smith (1977).

Q1158–187 Line list from Webb (1987). Redshift from Kunth, Sargent & Kowal (1981). Flux from Adam (1985).

Q1448–232 Line list from Webb (1987). Redshift from Espey et al. (1989). Flux and α measured from Wilkes et al. (1983), although a wide range of values exist in the literature and so a larger error (0.6 magnitudes in the flux) was used in section 4.2.

Q2000–330 Line list from Carswell et al. (1987). Redshift this paper (section 2.4). Flux and α measurements from Sargent, Steidel & Boksenberg (1989).

Q2204–573 Line list from Webb (1987). Redshift from Wilkes et al. (1983). V magnitude from Adam (1985).

Q2206–199 Line list from Rauch et al. (1993). Redshift this paper (section 2.4). V magnitude from Hewitt & Burbidge (1989).

Table 2 also gives an estimate of the relative effect of the different corrections made here. Each row gives the typical change in $\log(J_{23})$ that would be estimated using that quasar alone, with a typical absorption cloud 2 Mpc from the quasar ($q_0 = 0.5, H_0 = 100 \,\mathrm{km\,s}^{-1}$). The correction to obtain the systemic redshift is not necessary for any quasar whose redshift has been determined using low ionization lines. In such

| Object | N | | z | | Number |
name	Low	High	Low	High	of lines
Q0000–263	14.00	16.00	3.1130	3.3104	62
			3.4914	4.1210	101
Q0014+813	13.30	16.00	2.7000	3.3800	191
Q0207–398	13.75	16.00	2.0765	2.1752	11
			2.4055	2.4878	7
			2.6441	2.7346	6
			2.6852	2.7757	9
			2.7346	2.8180	8
Q0420–388	13.75	16.00	2.7200	3.0800	73
Q1033–033	14.00	16.00	3.7000	3.7710	16
			3.7916	3.8944	21
			3.9191	4.0301	24
			4.0548	4.1412	25
			4.1988	4.3139	30
			4.3525	4.4490	23
			4.4517	4.4780	2
Q1100–264	12.85	16.00	1.7886	1.8281	2
			1.8330	1.8733	8
			1.8774	1.9194	13
			1.9235	1.9646	9
			1.9696	2.0123	10
			2.0189	2.0617	6
			2.0683	2.1119	18
Q1158–187	13.75	16.00	2.3397	2.4510	9
Q1448–232	13.75	16.00	2.0847	2.1752	9
Q2000–330	13.75	16.00	3.3000	3.4255	23
			3.4580	3.5390	15
			3.5690	3.6440	18
			3.6810	3.7450	11
Q2204–573	13.75	16.00	2.4467	2.5371	10
			2.5454	2.6276	12
			2.6441	2.7280	8
Q2206–199	13.30	16.00	2.0864	2.1094	2
			2.1226	2.1637	8
			2.1760	2.2188	5
			2.2320	2.2739	7
			2.2887	2.3331	7
			2.3471	2.3940	10
			2.4105	2.4574	4
			2.4754	2.5215	11
Total: 11 quasars					844

Table 3. Completeness limits.

Variable	Without Inv. Eff. Statistic	Prob.	With Inv. Eff. Statistic	Prob.
N	1.11	0.17	1.05	0.22
z	1.12	0.16	1.05	0.22

Table 4. The K–S statistics measuring the quality of the fit.

cases the value given is the expected change if the redshift measurement had not been available.

Using the systematic redshift always reduces the background estimate, while correcting for reddening always acts in the opposite sense. The net result, in the final column of table 2, depends on the relative strength of these two factors. For most objects the redshift correction dominates, lowering $\log(J_{23})$ by ~ 0.15 (a decrease of 30%), but for four objects the reddening is more important (Q0014+813, the most reddened, has $B - V = 0.33$; the average for all other objects is 0.09).

Figure 3 shows the distribution of column density, N, and redshift, z, for the lines in the sample. The completeness limit was taken from the literature and depends on the quality of the spectra. There is also a clear trend with redshift as the number density increases and weak lines become less and less easy to separate in complex blends, whatever the data quality (see section 2.2 for a more detailed discussion of line blending).

4 FIT QUALITY AND ERROR ESTIMATES

4.1 The Quality of the Fit

Figures 4 and 5 show the cumulative data and model for each variable using two models: one includes the proximity effect (model **B**), one does not (model **A**). The probabilities of the associated K–S statistics are given in table 4. For the column density plots the worst discrepancy between model and data occurs at $\log(N) = 14.79$. The model with the proximity effect (to the right) has slightly more high column density clouds, as would be expected, although this is difficult to see in the figures (note that the dashed line — the model — is the curve that has changed). In the redshift plots the difference between the two models is more apparent because the changes are confined to a few redshifts, near the quasars, rather than, as in the previous figures, spread across a wide range of column densities. The apparent difference between model and data is larger for the model that includes the proximity effect (on the right of figure 5). However, this is an optical illusion as the eye tends to measure the vertical difference between horizontal, rather than diagonal, lines. In fact the largest discrepancy in the left figure is at $z = 3.323$, shifting to $z = 3.330$ when the proximity effect is included. It is difficult to assess the importance of individual objects in cumulative plots, but the main difference in the redshift figure occurs near the redshift of Q0014+813. However, since this is also the case without the proximity effect (the left–hand figure) it does not seem to be connected to the unusually large flux correction for this object (section 3).

In both cases — with and without the proximity effect — the model fits the data reasonably well. It is not surprising that including the proximity effect only increases the acceptability of the fit slightly, as the test is dominated by the majority of lines which are not influenced by the quasar. The likelihood ratio test that we use in section 6.2.1 is a more powerful method for comparing two models, but can only be used if the models are already a reasonable fit (as shown here).

4.2 Sources of Error

There are two sources of stochastic uncertainty in the values of estimated parameters: the finite number of observations and the error associated with each observation (column densities, redshifts, quasar fluxes, etc.).

The first source of variation — the limited information available from a finite number of observations — can be assessed by examining the distribution of the posterior probabilities for each parameter. This is described in the following section.

The second source of variation — the errors associated with each measurement — can be assessed by repeating the analysis for simulated sets of data. In theory these errors could have been included in the model and their contribution would have been apparent in the posterior distribution. In practice there was insufficient information or computer time to make a detailed model of the error distribution.

Instead, ten different sets of line–lists were created. Each was based on the original, with each new value, X, calculated from the observed value x and error estimate σ_X:

$$X = x + a\sigma_X \ , \tag{15}$$

where a was selected at random from a (approximate) normal distribution with zero mean and unit variance. The redshift (standard error 0.003) and luminosity (standard error 0.2 magnitudes) of each background quasar were also changed. For Q0420–388 the redshift error was increased to 0.1 and, for Q1448–232, the magnitude error was increased to 0.6 magnitudes. The model was fitted to each data set and the most likely values of the parameters recorded. A Gaussian was fitted to the distribution of values. In some cases (eg. figure 8) a Gaussian curve may not be the best way to describe the distribution of measurements. However, since the error in the parameters is dominated by the small number of data points, rather than the observational errors, using a different curve will make little difference to the final results.

Since the two sources of stochastic error are not expected to be correlated they can be combined to give the final distribution of the parameters. The Gaussian fitted to the variation from measurement errors is convolved with the posterior distribution of the variable. The final, normalized distribution is then a good approximation to the actual distribution of values expected.

This procedure is shown in figures 6 to 8. For each parameter in the model the 'raw' posterior distribution is plotted (thin line and points). The distribution of values from the synthetic data is shown as a dashed histogram and the fitted Gaussian is a thin line. The final distribution, after convolution, is the heavy line. In general the uncertainties due to a finite data set are the main source of error.
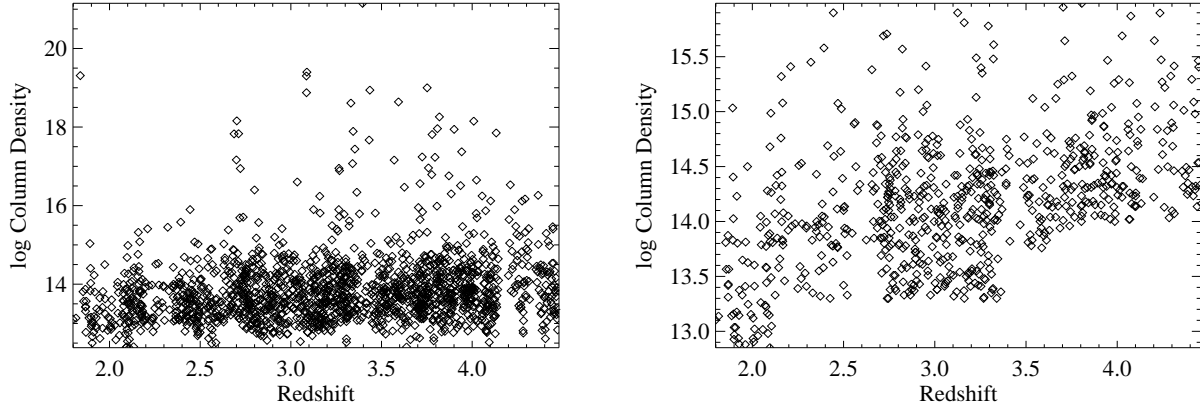
Figure 3. The lines in the full sample (left) used to calculate the attenuation of the quasar flux by intervening clouds and the restricted sample (right) to which the model was fitted.
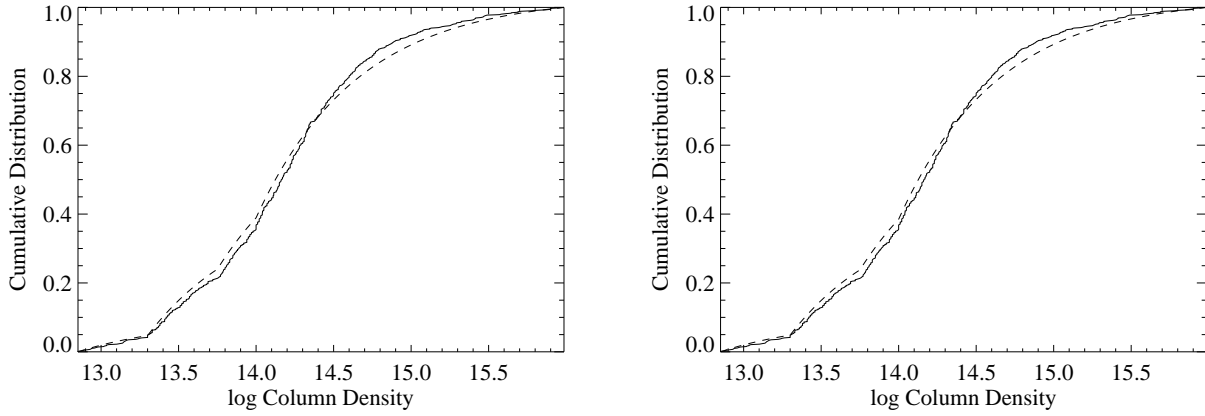

Figure 4. The cumulative data (solid line) and model (dashed), integrating over z, for the lines in the sample, plotted against column density ($\log(N)$). The model on the right includes the proximity effect.
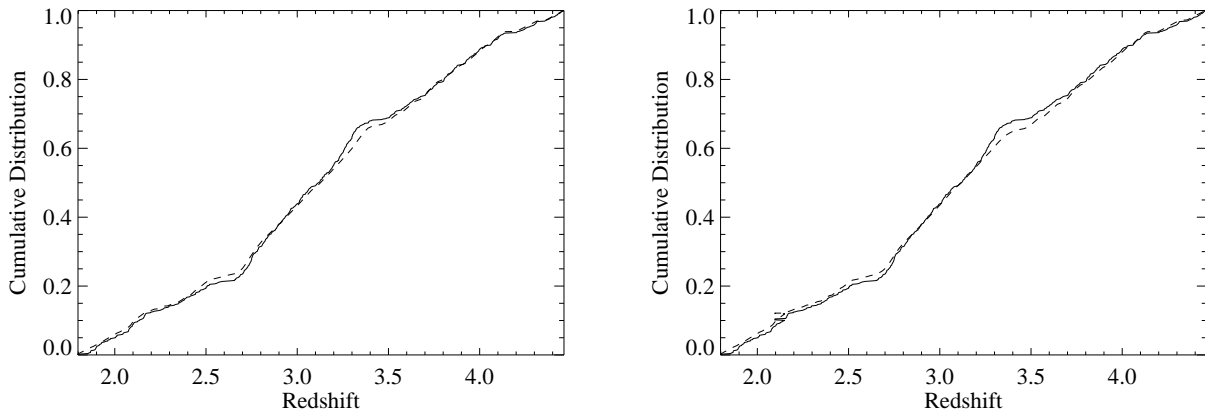

Figure 5. The cumulative data (solid line) and model (dashed), integrating over N, for the lines in the sample, plotted against redshift. The model on the right includes the proximity effect.

4.3 Error Estimates from Posterior Probabilities

If $p(\mathbf{y}|\theta)$ is the likelihood of the observations ($\mathbf{y}$), given the model (with parameters θ), then we need an expression for the posterior probability of a 'parameter of interest', η. This might be one of the model parameters, or some function of the parameters (such as the background flux at a certain redshift):

$$\eta = g(\theta) \ . \tag{16}$$

For example, the value of J_{23} at a particular redshift for models **C** to **E** in section 2.1 is a linear function of several parameters (two or more of $J_{3.25}, J_{z_B}, \alpha_1,$ and α_2). To calculate how likely a particular flux is the probabilities of all the possible combinations of parameter values consistent with that value must be considered: it is necessary to integrate over all possible values of β and γ', and all values of $J_{z_B}, \alpha_1,$ etc. which are consistent with $J_{23}(z)$ having that value.

In other words, to find the posterior distribution of η, $\pi(\eta|\theta)$, we must marginalise the remaining model parameters:

$$\pi(\eta|\theta) = \lim_{\gamma \to 0} \frac{1}{\gamma} \int_D \pi(\theta|\mathbf{y}) \, d\theta \ , \tag{17}$$

where D is the region of parameter space for which $\eta \leq g(\theta) \leq \eta + \gamma$ and $\pi(\theta|\mathbf{y}) \propto \pi(\theta)p(\mathbf{y}|\theta)$, the posterior density of θ with prior $\pi(\theta)$.

A uniform prior is used here for all parameters (equivalent to normal maximum likelihood analysis). Explicitly, power law exponents and the logarithm of the flux have prior distributions which are uniform over $[-\infty, +\infty]$.

Doing the multi–dimensional integral described above would require a large (prohibitive) amount of computer time. However, the log–likelihood can be approximated by a second order series expansion in θ. This is equivalent to assuming that the other parameters are distributed as a multivariate normal distribution, and the result can then be calculated analytically. Such a procedure is shown, by Leonard, Hsu & Tsui (1989), to give the following procedure when $g(\theta)$ is a linear function of θ:

$$\bar{\pi}(\eta|\mathbf{y}) \propto \frac{\pi_M(\eta|\mathbf{y})}{|\mathbf{R}_\nu|^{1/2}(b_\nu{}^T \mathbf{R}_\nu{}^{-1} b_\nu)^{1/2}} \ , \tag{18}$$

where

$$\pi_M(\eta|\mathbf{y}) = \sup_{\theta:g(\theta)=\eta} \pi(\theta|\mathbf{y}) \tag{19}$$

$$= \pi(\theta_\eta|\mathbf{y}) \ , \tag{20}$$

$$b_\nu = \left. \frac{\partial g(\theta)}{\partial \theta} \right|_{\theta=\theta_\eta} , \tag{21}$$

$$\mathbf{R}_\nu = \left. \frac{\partial^2 \ln \pi(\theta|\mathbf{y})}{\partial(\theta\theta^T)} \right|_{\theta=\theta_\eta} . \tag{22}$$

The likelihood is maximised with the constraint that $g(\theta)$ has a particular value. $\mathbf{R}_\nu$ is the Hessian matrix used in the fitting routine (Press et al. 1992) and b_ν is known (when η is the average of the first two of three parameters, for example, $b_\nu = 0.5, 0.5, 0$).

This quickens the calculation enormously. To estimate the posterior distribution for, say, J_{23}, it is only necessary to choose a series of values and, at each point, find the best fit consistent with that value. The Hessian matrix, which is

returned by many fitting routines, can then be used — following the formulae above — to calculate an approximation to the integral, giving a value proportional to the probability at that point. Once this has been repeated for a range of different values of J_{23} the resulting probability distribution can be normalised to give an integral of one.

Note that this procedure is only suitable when $g(\theta)$ is a linear function of θ — Leonard, Hsu & Tsui (1989) give the expressions needed for more complex parameters.

5 RESULTS

A summary of the results for the different models is given in table 5. The models are:

A — No Proximity Effect. The population model described in section 2, but without the proximity effect.

B — Constant Background. The population model described in section 2 with a constant ionising background.

C — Power Law Background. The population model described in section 2 with an ionising background which varies as a power law with redshift

D — Broken Power Law Background. The population model described in section 2 with an ionising background whose power law exponent changes at $z_B = 3.25$.

E — Correction for Extinction in Damped Systems. As **D**, but with a correction for absorption in known damped absorption systems (section 2.3.2).

In this paper we assume $q_0 = 0.5$ and $H_0 = 100 \, \mathrm{km \, s^{-1}/Mpc}$.

5.1 Population Distribution

The maximum likelihood 'best–fit' values for the parameters are given in table 5. The quoted errors are the differences (a single value if the distribution is symmetric) at which the probability falls by the factor $1/\sqrt{e}$. This is equivalent to a '1σ error' for parameters with normal error distributions.

The observed evolution of the number of clouds per unit redshift is described in the standard notation found in the literature

$$dN/dz = A_0(1 + z)^\gamma \ . \tag{23}$$

The variable used in the maximum likelihood fits here, γ', excludes variations expected from purely cosmological variations and is related to γ by:

$$\gamma = \begin{cases} \gamma' + 1 & \text{if } q_0 = 0 \\ \gamma' + \frac{1}{2} & \text{if } q_0 = 0.5 \ . \end{cases} \tag{24}$$

Figure 9 shows the variation in population parameters for model **D** as the completeness limits are increased in steps of $\Delta \log(N) = 0.1$. The number of clouds decreases from 844 to 425 (when the completeness levels have been increased by $\Delta \log(N) = 0.5$).

5.2 Ionising Background

Values of the ionising flux parameters are show in table 5. The expected probability distributions for models **B** and **D** are shown in figures 7 and 8. The background flux relation is described in section 2.1.
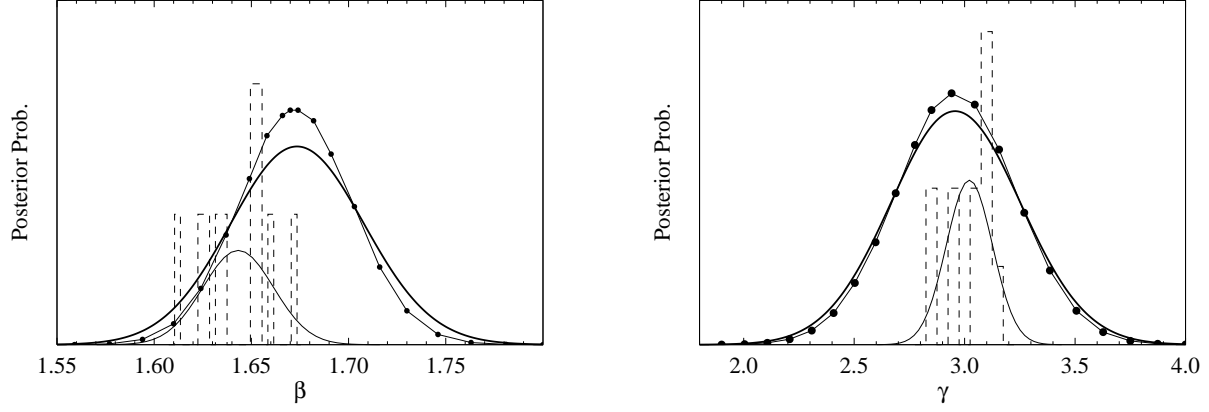
Figure 6. The expected probability distribution of the model parameters β and γ (heavy line) for model **D**. The dashed histogram and Gaussian (thin line) show how the measured value varies for different sets of data. The dash-dot line shows the uncertainty in the parameter because the data are limited. These are combined to give the final distribution (bold). See section 4.2 for mode details.
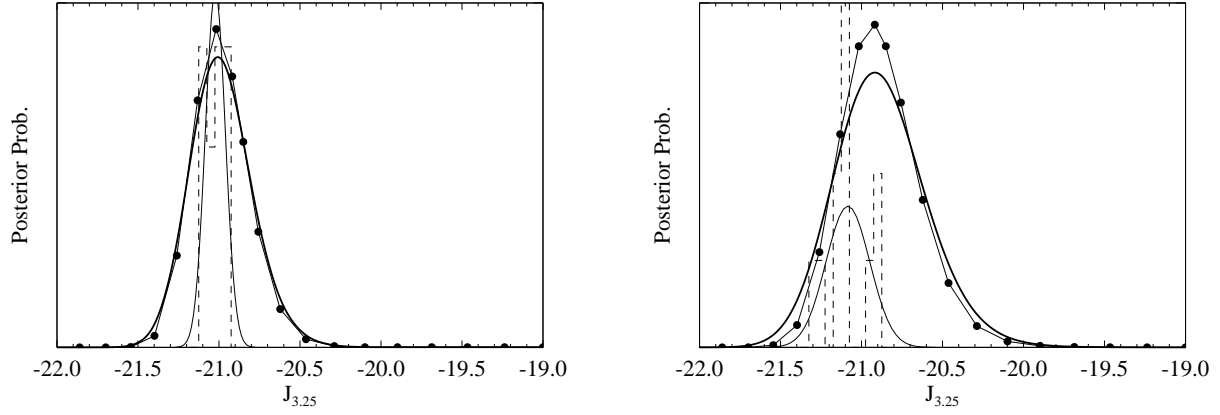

Figure 7. The expected probability distribution of the log background flux at $z = 3.25$ (heavy line) for models **B** (left) and **D**. The uncertainty from the small number of lines near the quasar (line with points) is significantly larger than that from uncertainties in column densities or quasar properties (thin curve). See section 4.2 for a full description of the plot.
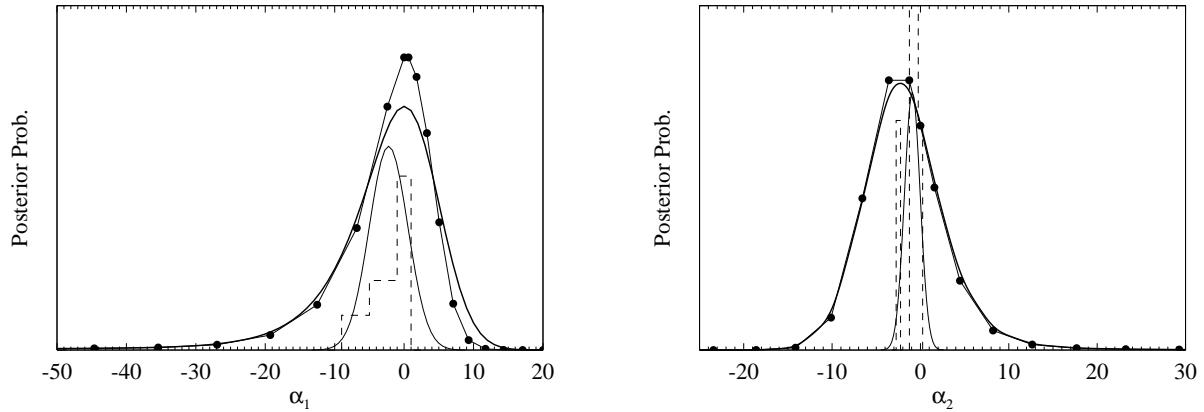

Figure 8. The expected probability distribution of the model parameters α_1 and α_2 (heavy line) for model **D**. See section 4.2 for a full description of the plot.

Model	β		γ		J_{z_B}		α_1		α_2		z_B	-2 log–likelihood
A	1.66	±0.03	2.7	±0.3		No background						60086.2
B	1.67	±0.03	2.9	±0.3	-21.0	±0.2						60052.8
C	1.67	±0.03	3.0	±0.3	-21.0	±0.2	-1	±3				60052.6
D	1.67	±0.04	3.0	±0.3	-20.9	±0.3	0	$+5,-6$	-2	±4	3.25	60052.4
E	1.67	±0.03	3.0	±0.3	-20.9	$+0.3,-0.2$	0	$+5,-6$	-2	$+7,-4$	3.25	60051.4

Table 5. The best–fit parameters and expected errors for the models.
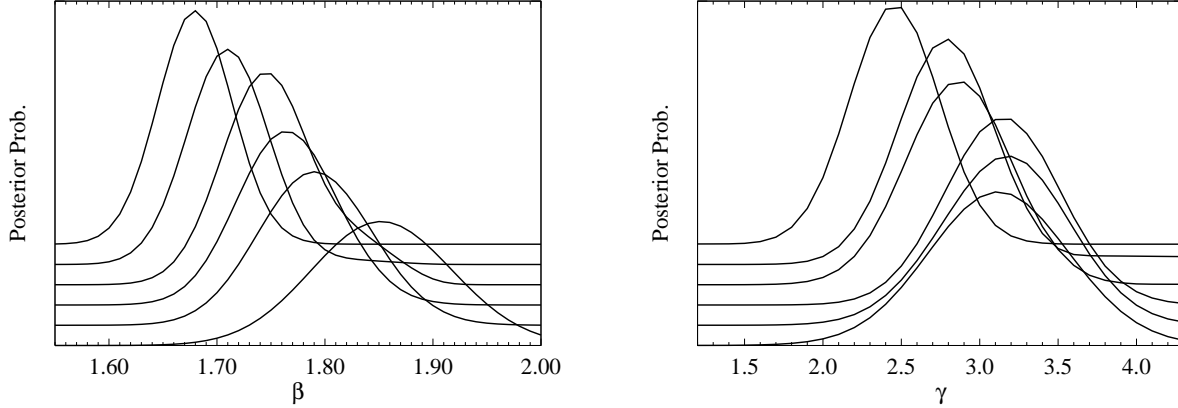
Figure 9. The expected probability distribution of the population parameters for model **D**. The top curve is for all data, each lower curve is for data remaining when the column density completeness limits are progressively increased by $\Delta\log(N) = 0.1$.

The variables used to describe the variation of the flux with redshift are strongly correlated. To illustrate the constraints more clearly the marginalised posterior distribution (section 4.3) of J_{23} was calculated at a series of redshifts. These are shown (after convolution with the combination of Gaussians appropriate for the uncertainties in the parameters from observational errors) for model **D** in figure 10. The distribution at each redshift is calculated independently. This gives a conservative representation since the marginalisation procedure assumes that parameters can take all possible values consistent with the background at that redshift (the probability that the flux can be low at a certain redshift, for example, includes the possibility that it is higher at other redshifts). Figure 10 also compares the results from the full data set (solid lines and smaller boxes) with those from the data set with column density completeness limits raised by $\Delta\log(N) = 0.5$ (the same data as the final curves in figure 9).

Table 6 gives the most likely flux (at probability p_m), an estimate of the '1σ error' (where the probability drops to $p_m/\sqrt{e}$), the median flux, the upper and lower quartiles, and the 5% and 95% limits for model **D** at the redshifts shown in figure 10. It is difficult to assess the uncertainty in these values. In general the central measurements are more reliable than the extreme limits. The latter are more uncertain for two reasons. First, the distribution of unlikely models is more likely to be affected by assumptions in section 4.3 on the normal distribution of secondary parameters. Second, the tails of the probability distribution are very flat, making the flux value sensitive to numerical noise. Extreme limits, therefore, should only be taken as a measure of the relevant flux magnitude. Most likely and median values are given to

	$z=2$	$z=2.5$	$z=3$	$z=3.5$	$z=4$	$z=4.5$
$p_m/\sqrt{e}$	30	50	60	60	40	30
p_m	137	129	118	103	80	63
$p_m/\sqrt{e}$	1000	400	220	180	160	170
5%	10	30	50	40	30	20
25%	70	80	80	70	60	40
50%	232	172	124	108	87	75
75%	1000	400	200	160	100	200
95%	30000	3000	400	300	400	600

Table 6. The fluxes (J_{23}) corresponding to various posterior probabilities for model **D**. See the text for details on the expected errors in these values.

the nearest integer to help others plot our results — the actual accuracy is probably lower.

6 DISCUSSION

6.1 Population Parameters

Parameter values for the different models are given in table 5. They are generally consistent with other estimates (Lu, Wolfe & Turnshek 1991; Rauch et al. 1993). Including the proximity effect increases γ by ~ 0.2. Although not statistically significant, the change is in the sense expected, since local depletions at the higher redshift end of each data set are removed.

Figure 9 shows the change in population parameters as the completeness limits for the observations are increased. The most likely values (curve peaks) of both β and γ increase as weaker lines are excluded, although γ decreases again for the last sample.

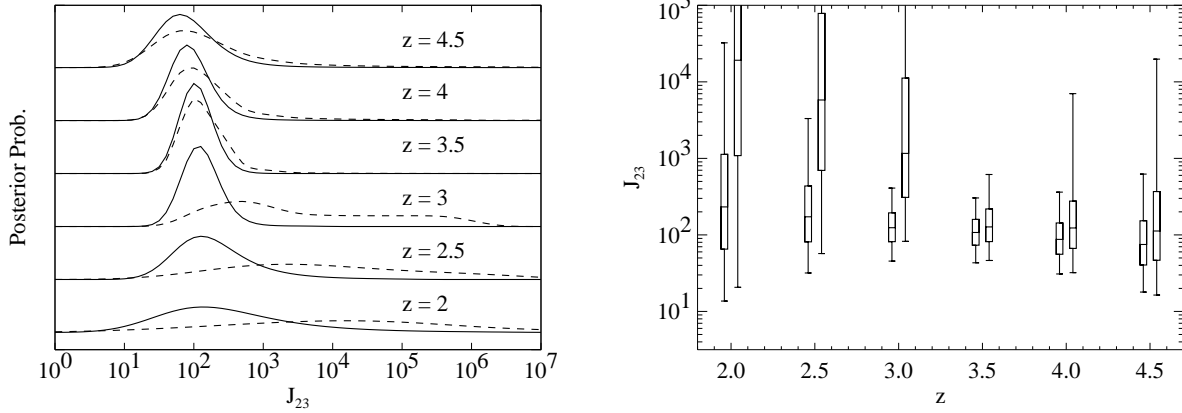The value of β found here (~ 1.7) is significantly differ-

Figure 10. The expected probability distribution of the log background flux for model **D**, comparing the results from the full data set with those obtained when the column density completeness limit is raised by $\Delta \log(N) = 0.5$ (dashed line, left; larger boxes, right). The box plots show median, quartiles, and 95% limits.

ent from that found by Press & Rybicki (1993) ($\beta \sim 1.4$) using a different technique (which is insensitive to Malmquist bias and line blending). The value of β moves still further away as the column density completeness limits are increased. This is not consistent with Malmquist bias, which would give a smaller change in β (section 2.2), but could be a result of either line blending or a population in which β increases with column density. The latter explanation is also consistent with Cristiani et al. (1995) who found a break in the column density distribution with $\beta = 1.10$ for $\log(N) < 14.0$, and $\beta = 1.80$ above this value. Later work (Giallongo et al. 1996, see section 6.3.1) confirmed this.

Recent work by Hu et al. (1995), however, using data with better signal–to–noise and resolution, finds that the distribution of column densities is described by a single power law ($\beta \sim 1.46$) until $\log(N) \sim 12.3$, when line blending in in their sample becomes significant. It might be possible that their sample is not sufficiently large (66 lines with $\log(N) > 14.5$, compared with 192 here) to detect a steeper distribution of high column density lines.

The change in γ as completeness limits are raised may reflect the decrease in line blending at higher column densities. This suggests that the value here is an over–estimate, although the shift is within the 95% confidence interval. No estimate is significantly different from the value of 2.46 found by Press & Rybicki (1993) (again, using a method less susceptible to blending problems).

6.2 The Proximity Effect

6.2.1 Is the Proximity Effect Real?

The likelihood ratio statistic (equivalent to the 'F test'), comparing model **A** with any other, indicates that the null hypothesis (that the proximity effect, as described by the model here, should be disregarded) can be rejected with a confidence exceeding 99.9%. Note that this confirmation is based on the likelihood values in table 5. This test is much more powerful than the K–S test (section 4.1) which was only used to see whether the models were sufficiently good for the likelihood ratio test to be used.

To reiterate: if model **A** and model **B** are taken as competing descriptions of the population of Lyman–α clouds, then the likelihood ratio test, which allows for the extra degree of freedom introduced, strongly favours a description which includes the proximity effect. The model without the proximity effect is firmly rejected. This does not imply that the interpretation of the effect (ie. additional ionization by background radiation) is correct, but it does indicate that the proximity effect, in the restricted, statistical sense above, is 'real' (cf. Röser 1995).

If the assumptions behind this analysis are correct, in particular that the proximity effect is due to the additional ionising flux from the quasar, then the average value of the background is $100\,^{+50}_{-30}$ J$_{23}$ (model **B**).

If a more flexible model for the background (two power laws) is used the flux is consistent with a value of $120\,^{+110}_{-50}$ J$_{23}$ (model **D** at $z = 3.25$).

6.2.2 Systematic Errors

Five sources of systematic error are discussed here: Malmquist bias and line blending; reddening by damped absorption systems; increased clustering of clouds near quasars; the effect of gravitational lensing.

The constraints on the background given here may be affected by Malmquist bias and line blending (sections 2.2 and 6.1). The effects of line blending will be discussed further in section 6.3.2, where a comparison with a different procedure suggests that it may cause us to over–estimate the flux (by perhaps 0.1 dex). Malmquist bias is more likely to affect parameters sensitive to absolute column densities than those which rely only on relative changes in the observed population. So while this may have an effect on β, it should have much less influence on the inferred background value.

Attenuation by intervening damped absorption systems will lower the apparent quasar flux and so give an estimate for the background which is too low. This is corrected in model **E**, which includes adjustments for the known damped systems (section 2.3.2, table 1). The change in the inferred

background flux is insignificant (figure 12, table 5), implying that the magnitude of the bias is less than 0.1 dex.

If quasars lie in regions of increased absorption line clustering (Loeb & Eisenstein 1995; Yurchenko, Lanzetta & Webb 1995) then the background flux may be overestimated by up to 0.5, or even 1, dex.

Gravitational lensing may change the apparent brightness of a quasar — in general the change can make the quasar appear either brighter or fainter. Absorption line observations are made towards the brightest quasars known (to get good quality spectra). Since there are more faint quasars than bright ones this will preferentially select objects which have been brightened by lensing (see the comments on Malmquist bias in section 2.2). An artificially high estimate of the quasar flux will cause us to over–estimate the background.

Unfortunately, models which assess the magnitude of the increase in quasar brightness are very sensitive to the model population of lensing objects. From Pei (1995) an upper limit consistent with observations is an increase in flux of about 0.5 magnitudes, corresponding to a background estimate which is too high by a factor of 1.6 (0.2 dex). The probable effect, however, could be much smaller (Blandford & Narayan 1992).

If bright quasars are more likely to be lensed we can make a rudimentary measurement of the effect by splitting the data into two separate samples. When fitted with a constant background (model **B**) the result for the five brightest objects is indeed brighter than that for the remaining six, by 0.1 dex. The errors, however, are larger (0.3 dex), making it impossible to draw any useful conclusions.

The effects of Malmquist bias, line blending and damped absorption systems are unlikely to change the results here significantly. Cloud clustering and gravitational lensing could be more important — in each case the background would be over–estimated. The magnitude of these last two biases is not certain, but cloud clustering seems more likely to be significant.

6.2.3   *Is there any Evidence for Evolution?*

More complex models allow the background flux to vary with redshift. If the flux does evolve then these models should fit the data better. However, there is no significant change in the fit when comparing the likelihood of models **C** to **E** with that of **B**. Nor are α_1 or α_2 significantly different from zero. So there is no significant evidence for a background which changes with redshift.

The asymmetries in the wings of the posterior distributions of α_1 or α_2 for model **D** (figure 8) are a result of the weak constraints on upper limits (see next section). The box plots in figure 10 illustrate the range of evolutions that are possible.

6.2.4   *Upper and Lower Limits*

While there is little evidence here for evolution of the background, the upper limits to the background flux diverge more strongly than the lower limits at the lowest and highest redshifts. Also, the posterior probability of the background is extended more towards higher values.

The background was measured by comparing its effect with that of the quasar. If the background were larger the quasar would have less effect and the clouds with $\Delta_F < 1$ would not need as large a correction to the observed column density for them to agree with the population as a whole. If the background was less strong then the quasars would have a stronger influence and more clouds would be affected.

The upper limit to the flux depends on clouds influenced by the quasar. Figure 11 shows how Δ_F changes with redshift and proximity to the background quasar. From this figure it is clear that the upper limit is dominated by only a few clouds. However, the lower limit also depends on clouds near to, but not influenced by, the quasar. This involves many more clouds. The lower limit is therefore stronger, more uniform, and less sensitive to the amount of data, than the upper limit.

Other procedures for calculating the errors in the flux have assumed that the error is symmetrical (the only apparent exception is Fernández–Soto et al. (1995) who unfortunately had insufficient data to normalize the distribution). While this is acceptable for β and γ, whose posterior probability distributions (figure 6) can be well–approximated by Gaussian curves, it is clearly wrong for the background (eg. figure 10), especially where there are less data (at the lowest and highest redshifts).

An estimate based on the assumption that the error is normally distributed will be biased in two ways. First, since the extended upper bound to the background has been ignored, it will underestimate the 'best' value. Second, since the error bounds are calculated from the curvature of the posterior distribution at its peak (ie. from the Hessian matrix) they will not take account of the extended 'tails' and so will underestimate the true range of values. In addition, most earlier work has calculated errors assuming that the other population parameters are fixed at their best–fit values. This will also under–estimate the true error limits. All these biases become more significant as the amount of data decreases.

The first of these biases also makes the interpretation of the box–plots (eg. figures 10 and 12) more difficult. For example, the curves in the left–hand plot in figure 10 and the data in table 6 show that the value of the flux with highest probability at $z = 2$ is 140 J_{23} (for model **D**). In contrast the box–plot on the right shows that the median probability is almost twice as large (230 J_{23}). Neither plot is 'wrong': this is the consequence of asymmetric error distributions.

6.3   **Comparison with Previous Estimates**

6.3.1   *Earlier High–Resolution Work*

Fernández–Soto et al. (1995) fitted high signal–to–noise data towards three quasars. For $2 < z < 2.7$ they estimate an ionizing background intensity of 32 J_{23}, with an absolute lower limit (95% confidence) of 16 J_{23} (figure 12, the leftmost cross). They were unable to put any upper limit on their results.

Cristiani et al. (1995) determined a value of 50 J_{23} using a sample of five quasars with a lower column density cut–off of $\log(N) = 13.3$. This sample was recently extended (Giallongo 1995). They find that the ionizing background is roughly constant over the range $1.7 < z < 4.0$ with a
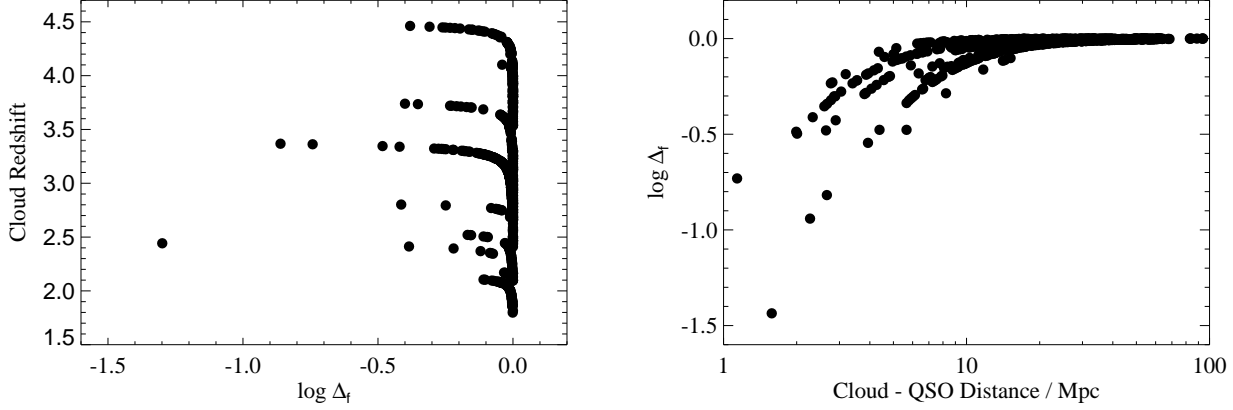
Figure 11. On the left, absorber redshifts are plotted against Δ_F. On the right Δ_F is plotted against the distance between cloud and quasar. Note that the correction for the quasar's flux, and hence the upper limit to the estimate of the background, is significant for only a small fraction of the clouds.
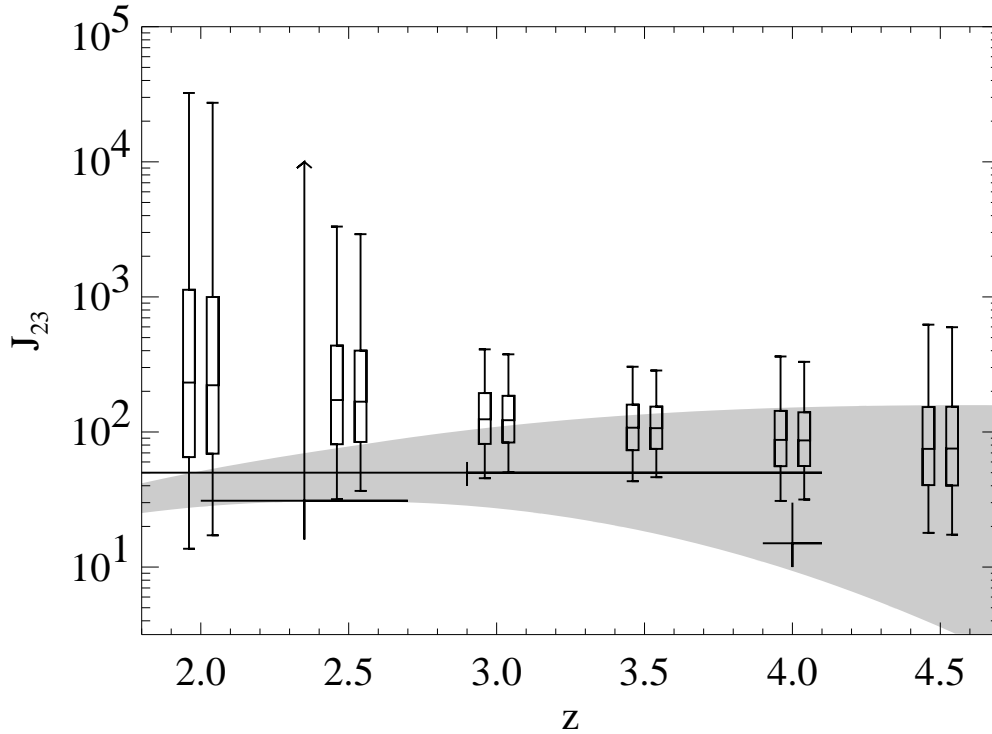

Figure 12. The expected probability distribution of the log background flux for models **D** (left) and **E** (right, including a correction for the known damped absorption systems). The box plots show median, quartiles, and 95% limits. The shaded area covers the range of backgrounds described in Fall & Pei (1995). The lower boundary is the expected background if all quasars are visible, the higher fluxes are possible if an increasing fraction of the quasar population is obscured at higher redshifts. The crosses and arrows mark the extent of previous measurements from high resolution spectra — see the text for more details.

value of 50 J_{23} which they considered a possible lower limit (figure 12, the middle lower limit).

While this paper was being refereed Giallongo et al. (1996) became available, extending the work above. Using a maximum likelihood analysis with an unspecified procedure for calculating errors they give an estimate for the back-ground of 50 ± 10 J_{23}. They found no evidence for evolution with redshift when using a single power law exponent.

Williger et al. (1994) used a single object, Q1033–033, which is included in this sample, to give an estimate of $10 - 30$ J_{23} (figure 12, the rightmost cross). The error limits are smaller than those found here, even though they only use

a subset of this data, which suggests that they have been significantly underestimated.

If the errors in Williger et al. (1994) are indeed underestimates then these measurements are consistent with the results here. However, the best–fit values are all lower than those found here. This may be, at least partly, because of the biases discussed in section 6.2.4.

Williger et al. (1994) used a more direct method than usual to estimate the background. This gives a useful constraint on the effect of line blending in the procedures used, and is explored in more detail below.

6.3.2 Q1033–033 and Line Blending

The measured value of the background, $80\,^{+80}_{-40}$ J_{23} (model **D** at $z = 4$), is larger than an earlier estimate using a subset of this data (Williger et al. 1994, Q1033–033, $10 - 30$ J_{23}).

As has already been argued, it is difficult to understand how a procedure using much less data could have smaller error limits than the results here, so it is likely that the error was an underestimate and that the two results are consistent. However, it is interesting to see if there is also a systematic bias in the analyses used.

The correction for galactic absorption is not very large for this object (about 20%). More importantly, the procedures used differ significantly in how they are affected by blended lines. These are a problem at the highest redshifts, where the increased Lyman–α cloud population density means that it is not always possible to resolve individual clouds. Williger et al. (1994) added additional lines ($\log(N) = 13.7$, $b = 30$ $\mathrm{km\,s^{-1}}$) to their $z = 4.26$ spectra of Q1033–033 and found that between 40% and 75% would be missed in the line list.

As the lower column density limit is raised Williger et al. (1994) find that the observed value of γ also increases. The resulting stronger redshift evolution would make the deficit of clouds near the quasar more significant and so give a lower estimate of the background. Although not significant at the 95% level, there is an indication that γ also increases with higher column density in this analysis (section 6.1, figure 9). While it is possible that γ varies with column density the same dependence would be expected if line blending is reducing the number of smaller clouds. To understand how line blending can affect the estimates, we will now examine the two analyses in more detail.

Line blending makes the detection of lines less likely. Near the quasar lines are easier to detect because the forest is more sparse. In the analysis used in this paper the appearance of these 'extra' lines reduces the apparent effect of the quasar. Alternatively, one can say that away from the quasar line blending lowers γ. Both arguments describe the same process and imply that the estimated background flux is too large.

In contrast, Williger et al. (1994) take a line–list from a crowded region, which has too few weak lines and correspondingly more saturated lines, and reduce the column densities until they agree with a region closer to the quasar. Since a few saturated lines are less sensitive to the quasar's flux than a larger number of weaker lines, the effect of this flux is over–estimated (and poorly determined), making the background seem less significant and giving a final value for the background flux which is too small. This method is

therefore biased in the opposite sense to ours and so the true value of the background probably lies between their estimate and ours.

The comparison with Williger et al. (1994) gives one estimate of the bias from line blending. Another can be made by raising the completeness limits of the data (section 2.2). This should decrease the number of weak, blended lines, but also excludes approximately half the data. In figure 10 the flux estimates from the full data set are shown together with those from one in which the limits have been raised by $\Delta \log(N) = 0.5$. There is little change in the lowest reasonable flux, an increase in the upper limits, and in increase in the 'best–fit' values. The flux for $z < 3$ is almost unconstrained by the restricted sample (section 6.2.4 explains the asymmetry).

An increase of 0.5 in $\log(N)$ is a substantial change in the completeness limits. That the lower limits remain constant (to within ~ 0.1 dex) suggests that line blending is not causing the flux to be significantly over–estimated. The increase in the upper limits is expected when the number of clouds in the sample decreases (section 6.2.4).

In summary, the total difference between our measurement and that in Williger et al. (1994) is 0.7 dex which can be taken as an upper limit on the effect of line blending. However, a more typical value, from the constancy of the lower limits when completeness limits are raised, is probably ~ 0.1 dex.

6.3.3 Results from Lower Resolution Spectra

Bechtold (1994) analysed lower resolution spectra towards 34 quasars using equivalent widths rather than individual column density measurements. She derived a background flux of 300 J_{23} ($1.6 < z < 4.1$), decreasing to 100 J_{23} when a uniform correction was applied to correct for non–systemic quasar redshifts. With low–resolution data a value of β is used to change from a distribution of equivalent widths to column densities. If β is decreased from 1.7 to a value closer to that found for narrower lines (see section 6.1) then the inferred background estimate could decrease further.

The evolution was not well–constrained ($-7 < \alpha < 4$). No distinction was made between the lower and upper constraints on the flux estimate, and it is likely that the wide range of values reflects the lack of strong upper constraints which we see in our analysis.

It is not clear to what extent this analysis is affected by line blending. Certainly the comments above — that relatively more clouds will be detected near the quasar — also apply.

6.3.4 Lower Redshift Measurements

The background intensity presented in this paper is much larger than the 8 J_{23} upper limit at $z = 0$ found by Vogel et al. (1995). Kulkarni & Fall (1993) obtain an even lower value of $0.6\,^{+1.2}_{-0.4}$ J_{23} at $z = 0.5$ by analysing the proximity effect in HST observations. However, even an unevolving flux will decrease by a factor of ~ 50 between $z = 2$ and 0, so such a decline is not inconsistent with the results given here.

6.4   What is the Source of the Background?

6.4.1   Quasars

Quasars are likely to provide a significant, if not dominant, contribution to the extragalactic background. An estimate of the ionizing background can be calculated from models of the quasar population. Figure 12 shows the constraints from models **D** and **E** and compares them with the expected evolution of the background calculated by Fall & Pei (1995). The background can take a range of values (the shaded region), with the lower boundary indicating the expected trend for a dust–free universe and larger values taking into account those quasars that may be hidden from our view, but which still contribute to the intergalactic ionizing flux. The hypothesis that the flux is only from visible quasars (the unobscured model in Fall & Pei 1995) is formally rejected at over the 95% significance level since the predicted evolution is outside the 95% bar in the box plots at higher redshift.

Although our background estimate excludes a simple quasar–dominated model based on the observed number of such objects, the analysis here may give a background flux which is biased (too large) from a combination of line blending (section 6.3.2) and clustering around the background quasars. From the comparison with Williger et al. (1994), above, there is an upper limit on the correction for line blending, at the higher redshifts, of 0.7 dex. However, an analysis of the data when column density completeness limits were increased by $\Delta \log(N) = 0.5$ suggests that a change in the lower limits here of ~ 0.1 dex is more likely. A further change of up to between 0.5 and 1 dex is possible if quasars lie in regions of increased clustering (section 6.2.2). These two effects imply that at the highest redshifts the flux measured here could reasonably overestimate the real value by ~ 0.5 dex. This could make the measurements marginally consistent with the expected flux from the observed population of quasars.

There is also some uncertainty in the expected background from quasars since observations could be incomplete even at the better understood lower redshifts (eg. Goldschmidt et al. 1992) and while absorption in damped systems is understood in theory (Fall & Pei 1993) its effect is uncertain (particularly because the distribution of high column density systems is poorly constrained).

The highest flux model (largest population of obscured quasars) from Fall & Pei (1995) is consistent with the measurements here (assuming that the objects used in this paper are not significantly obscured).

6.4.2   Stars

The background appears to be stronger than the integrated flux from the known quasar population. Can star formation at high redshifts explain the discrepancy?

Recent results from observations of low redshift starbursts (Leitherer et al. 1995) suggest that very few ionizing photons ($\leq 3\,\%$) escape from these systems. If high redshift starbursts are similar in their properties, then the presence of cool gas in these objects would similarly limit their contribution to the ionizing background. However, Madau & Shull (1996) estimate that if star formation occurs in Lyman–α clouds, and a significant fraction of the ionizing photons

($\sim 25\,\%$) escape, then these photons may contribute a substantial fraction of the ionizing background photons in their immediate vicinity. As an example, at $z \sim 3$ they estimate that $J_\nu \leq 50\, J_{23}$ if star formation sets in at $z \sim 3.2$. This flux would dominate the lowest (no correction for obscuration) quasar background shown in figure 12 and could be consistent with the intensity we estimate for the background at this redshift, given the possible systematic biases discussed above and in section 6.2.2.

7   CONCLUSIONS

A model has been fitted to the population of Lyman–α clouds. The model includes the relative effect of the ionising flux from the background and nearby quasars (section 2).

The derived model parameters for the population of absorbers are generally consistent with earlier estimates. There is some evidence that β, the column density power law population exponent, increases with column density, but could also be due to line blending (section 6.1).

The ionising background is estimated to be $100^{+50}_{-30}\, J_{23}$ (model **B**, section 5.2) over the range of redshifts ($2 < z < 4.5$) covered by the data. No strong evidence for evolution in the ionizing background is seen over this redshift range. In particular, there is no significant evidence for a decline for $z > 3$ (section 6.2.3). Previous results may have been biased (too low, with optimistic error limits — section 6.2.4).

Constraints on the evolution of the background are shown in figure 12. The estimates are not consistent with the background flux expected from the observed population of quasars (section 6.4). However, two effects are likely to be important. First, both line blending and increased clustering of clouds near quasars lead to the measured background being overestimated. Second, a significant fraction of the quasar population at high redshifts may be obscured. Since their contribution to the background would then be underestimated this would imply that current models of the ionizing background are too low. Both of these would bring the expected and measured fluxes into closer agreement. It is also possible that gravitational lensing makes the measurement here an overestimate of the true background.

The dominant source of errors in our work is the limited number of lines near the background quasar (eg. figures 7 and 11). Systematic errors are smaller and become important only if it is necessary to make standard (unobscured quasar) models for the background consistent with the lower limits presented here. Further data will therefore make the estimate here more accurate, although observational data are limited by confusion of the most numerous lower column density systems ($\log(N) < 13.0$) so it will remain difficult to remove the bias from line blending. An improvement in the errors for the highest redshift data points, or a determination of the shape of the ionizing spectrum (e.g. from He II/H I estimates in Lyman–α clouds) would help in discriminating between current competing models for the ionizing background. Finally, a determination of the background strength in the redshift range $0.5 < z < 2.0$ is still needed.

8 ACKNOWLEDGEMENTS

REFERENCES

Adam, G., 1985, A&AS, 61, 225

Atwood, B., Baldwin, J. A., & Carswell, R. F., 1985, ApJ, 292, 58

Baldwin, J. A., Ferland, G. J., Korista, K. T., et al, 1995, ApJ, 461, 664

Barcons, X., & Fabian, A. C., 1987, MNRAS, 224, 675

Barvainis, R., Tacconi, L., Antonucci, R., et al, 1994, Nature, 371, 586

Bechtold, J. B., 1993, The Environment and Evolution of Galaxies, Ed. Shull,J. M., & Thronson, H. A., 559

Bechtold, J. B., 1994, ApJS, 91, 1

Blandford, R. D., & Narayan, R., 1992, ARA&A, 30, 311

Bohlin, R. C., Savage, B. D., & Drake, J. F., 1978, ApJ, 224, 132

Boissé, P., & Bergeron, J., 1988, A&A, 192, 1

Cardelli, J. A., Clayton, G. C., & Mathis, J. S., 1989, ApJ, 345, 245

Carswell, R. F., 1995, QSO Absorption Lines. Ed. Meylan, G., 313

Carswell, R. F, Mountain, C. M., Robertson, D. J., et al, 1991, ApJ, 381, L5

Carswell, R. F., Webb, J. K., Baldwin, J. A., & Atwood, B., 1987, ApJ, 319, 709

Cen, R., Miralda–Escudé, J., & Ostriker, J. P., 1994, ApJ, 437, L9

Cooke, A. J., 1994, Thesis, Cambridge University

Cristiani, S., D'Odorico, S., Fontana, A., et al, 1995, MNRAS, 273, 1016

Diplas, A., & Savage, B. D., 1994, ApJ, 427, 274

Espey, B. R., & Junkkarinen, V. T., 1996, preparation

Espey, B. R., 1993, ApJ, 411, L59

Espey, B. R., Carswell, R. F., Bailey. J. A., Smith, et al, 1989, ApJ, 342, 666

Fall, S. M., & Pei, Y. C., 1993, ApJ, 402, 479

Fall, S. M., & Pei, Y. C., 1995, QSO Absorption Lines. Ed. Meylan, G., 23

Fernández–Soto, A., Barcons, X., Carballo, R., & Webb, J. K., 1995, MNRAS, 277, 235

Francis, P. J., 1993, ApJ, 407, 519

Gaskell, C. M., 1982, ApJ, 263, 79

Giallongo, E., 1995, Presentation at the workshop on Lyman–alpha lines held at the STScI, May 1995

Giallongo, E., Cristiani, S., D'Odorico, S., et al, 1996, Preprint (for publication in ApJ)

Goldschmidt, P., Miller, L., La Franca, F., & Cristiani, S., 1992, MNRAS, 256, L65

Haardt, F., & Madau, P., 1996, ApJ, 461, 20

Heckman, T. M., Thompson, K. L., Miley, K. G., & van Breugel, W., 1991, ApJ, 370, 78

Heiles, C., & Cleary, M. N., 1979, AuJPA, 47, 1

Hewitt, A., & Burbidge, G., 1989, ApJS, 69, 1

Hogan, C. J., 1987, ApJ, 316, L59

Hu, E. M., Kim, T. S., Cowie, L. L., & Songalia, A., 1995, AJ, 110, 1526

Kulkarni, V. P., & Fall, S. M., 1993, ApJ, 413, L67

Kunth, D., Sargent, W. L. W., & Kowal, C., 1981, A&AS, 44, 229

Leitherer, C., Ferguson, H. C., Heckman, T. M., & Lowenthal, J. D., 1995, ApJ, 454, L19

Leonard, T., Hsu, J. S. J., & Tsui, K. W., 1989, JASA, 84, 1051

Lockman, F. J., & Savage, B. D., 1995, ApJS, 97, 1

Loeb, A., & Eisenstein, D. J., 1995, ApJ, 448, 17

Lu, L., Wolfe, A. M., & Turnshek, D. A., 1991, ApJ, 367, 19

Madau, P., & Shull, J. M., 1996, ApJ, 457, 551

Miralda–Escudé, J., & Rees, M., 1993, MNRAS, 260, 617

Miralda–Escudé, J., 1993, MNRAS, 262, 273

Osmer, P. S., & Smith, M. G., 1977, ApJ, 213, 607

Osmer, P. S., 1979, ApJ, 227, 18

Osterbrock, D. E., 1989, Astrophysics of Gaseous Nebulae and Active Galactic Nuclei, University Science Books

Ostriker, J. P., & Ikeuchi, S., 1983, ApJ, 268, L63

Pei, Y. C., & Fall, S. M., 1995, ApJ, 454, 69

Pei, Y. C., 1992, ApJ, 395, 130

Pei, Y. C., 1995, ApJ, 440, 485

Petitjean, P., & Mücket, J. P., 1995, A&A, 295, L9

Petitjean, P., Webb, J. K., Rauch, M., et al, 1993, MNRAS, 262, 499

Press, W. H., & Rybicki, G. B., 1993, ApJ, 418, 585

Press, W. H., Teukolsky, S. A., Vetterling, W. T., & Flannery, B. P., 1992, Numerical Recipies in Fortran, Cambridge University Press

Rauch, M., Carswell, R. F., Webb, J. K., & Weymann, R. J., 1993, MNRAS, 260, 589

Röser, H. J., 1995, A&A, 299, 641

Rybicki, G. B., & Lightman, A. P., 1979, John Wiley & Sons

Sargent, W. L. W., Steidel, C. C., & Boksenberg, A., 1989, ApJS, 69, 703

Sargent, W. L. W., Young, P. J., Boksenberg, A., & Tytler, A., 1980, ApJS, 42, 41

Stark, A. A., Gammie, C. F., Wilson, R. W., et al, 1992, ApJS, 79, 77

Tytler, D., & Fan, X. M., 1992, ApJS, 79, 1

Vishniac, E. T., & Bust, G. S., 1987, ApJ, 319, 14

Vogel, S. N., Weymann, R., Rauch, M., & Hamilton, T., 1995, ApJ, 441, 162

Webb, J. K., 1987, Thesis, Cambridge University

Wilkes, B. J., 1984, MNRAS, 207, 73

Wilkes, B. J., Wright, A. E., Jauncey, D. L., & Peterson, B. A., 1983, PASA, 5, 2

Williger, G. M., Baldwin, J. A., Carswell, R. F., et al, 1994, ApJ, 428, 574

Wolfe, A. M., Lanzetta, K. M., Foltz, C. B., & Chaffee, F. H., 1995, ApJ, 454, 698

Yurchenko, A. V., Lanzetta, K. M., & Webb, J. K., 1995, BAAS, 186, 45.04

Zhang, Y., Anninos, P., & Norman, M. L., 1995, ApJ, 453, L57